Electronic Supplementary Material (ESI) for Sustainable Energy & Fuels.
This journal is © The Royal Society of Chemistry 2020

Supplementary information

Are MXenes Suitable as Cathode Materials for Rechargeable Mg Batteries?

Henning Kaland,‡[a] Jacob Hadler-Jacobsen,‡[a] Frode Håskjold Fagerli,‡[a] Nils P. Wagner,[ab] Zhaohui Wang,[ac] Sverre M. Selbach,[a] Fride Vullum-Bruer,[a,d] Kjell Wiik*[a] and Sondre Kvalvåg Schnell*[a]

[a] Department of Materials Science and Engineering, NTNU Norwegian University of Science and Technology, NO-7491 Trondheim, Norway.
[b] SINTEF Industry, Sustainable Energy Technology, NO-7465 Trondheim, Norway.
[c] SINTEF Industry, Metal Production and Processing, NO-7465 Trondheim, Norway.
[d] SINTEF Energy Research, Thermal Energy, NO-7465 Trondheim, Norway.
E-mail: kjell.wiik@ntnu.no, sondre.k.schnell@ntnu.no
‡ These authors contributed equally to this work.

Experimental section

MAX phase preparation (Ti_3AlC_2 and V_2AlC)

Commercial Ti_3AlC_2 MAX phase was bought from Laizhou Kai Kai Ceramic Material Co., Ltd, while the V_2AlC MAX phase was synthesized through a solid state reaction of elemental precursor powders[1]; vanadium (99.5%, 325 mesh, Sigma-Aldrich), aluminium (99.5%, 325 mesh, Alfa Aesar) and graphite (99.5%, 400 mesh, TIMCAL TIMREX). The powders were mixed in a molar ratio V:Al:C of 2:1.3:1 and mixed by wet ball milling for 18 h in an isopropanol dispersion. After evaporation of the isopropanol with the aid of a rotavapor (Büchi R210), the powder mixture was pressed into cylindrical 1 g pellets, put in an alumina crucible, inserted into a sealed tube furnace (Entech ETF 17) and heat treated at 1500 °C in an argon atmosphere. The heating program was initiated with a 1 h flushing step to remove oxygen from the tube, before the chamber was heated with a heating rate of 5 °C/min, held at the final temperature for 4 h, and then cooled to room temperature at the same rate. After the heat treatment, the pellets were ground down to powders using a steel mortar. To further reduce the particle size and narrow the particle size distribution, both MAX phase powders (Ti_3AlC_2 and V_2AlC) were planetary milled (Retsch PM 100) using a 125 ml tungsten carbide (WC) milling jar, 11 WC milling balls with a diameter of 7 mm and an amount of isopropanol to just cover the milling balls. Both MAX phases were milled at 300 rpm. 10 g of the Ti_3AlC_2 MAX phase was milled for 135 min, while 3 g of the V_2AlC was milled for 6 hours to achieve the desired particle size and size distribution of the two powders (Figure S1).

MAX phase etching ($Ti_3C_2T_x$ and V_2CT_x)

The two MXenes were synthesized by exfoliation of the precursor MAX phases in aqueous HF solutions, based on previous work. [1, 2] After the milling process, 2.5 g of the Ti_3AlC_2 and V_2AlC powders were immersed in plastic beakers containing 50 ml of 10 wt% and 48 wt% HF solutions, respectively. In order to prevent excess heating and H_2 gas formation at the beginning of the etching, the powders were added slowly over a minimum of 15 minutes. After all the MAX phase powder was added, the plastic beakers were covered with parafilm to limit the evaporation during the etching process. However, in order to prevent build-up of H_2 gas inside the beaker, small holes were made in the parafilm. Then, the dispersions containing the Ti_3AlC_2 and V_2AlC powders were stirred using Teflon coated magnets at room temperature for 24 and 96 hours, respectively, in order to completely remove the aluminium from the parent MAX phases. After the etching process, the

powders were washed with deionized water in 125 ml plastic bottles, through several steps of centrifugation, decantation and dilution, to remove HF and other etching side products. This was continued until the dispersions had a pH > 5 (usually 5 times). The centrifugation was done using a VWR Mega Star 600 using an rpm of 4350 for 7 minutes, including a slow acceleration and deceleration time. Finally, to remove residual water, the powders were vacuum filtered using 0.22 µm pore sized hydrophilic Durapore membrane filters and dried under vacuum at 120 °C for 24 hours in a vacuum oven (Binder VD 23). After drying, the powders were scraped off the filter paper, and stored in glass sample bottles.

Materials characterization

The crystal structure of the synthesized materials was characterized by powder diffraction, conducted on a Bruker D8 Focus Diffractometer, utilizing a Cu Kα radiation source (ƛ = 1.5406 Å), a 0.2 mm divergence slit, a step size of 0.0143 and a dwelling time of 0.68 s between 2θ-values of 5° and 75°. The XRD measurements performed on the cathodes before and after cycling were done using inert sample holders, where the cathodes were held in place on a Si wafer with the aid of a small amount of vacuum grease. To characterize the particle sizes of the MAX phase powders, laser diffraction was conducted on a Horiba Partica LA-960, using isopropanol as the liquid medium and 2 minutes of sonication to break up agglomerates prior to the measurement. The particle morphology, microstructure and elemental composition was investigated by field emission scanning electron microscopy (LVFESEM, Zeiss SUPRA 55VP) equipped with energy dispersive X-ray spectroscopy (EDX). The morphology and microstructure were investigated with an acceleration voltage of 5 kV, whereas the EDX measurements were conducted at 15 kV. The reported EDX results are the average values of point scans on ten different particles.

Cathode preparation

Cathodes were prepared by mixing 80 wt% active material (120 mg), 10 wt% polyvinylidene fluoride binder (PVDF) (15 mg) and 10 wt% carbon black (15 mg) in 1 ml of 1-Ethyl-2-pyrrolidone (NEP) solvent, using a 5 ml steel shaker jar. A prepared solution of 5 wt% PVDF in NEP was used, in order to ensure a homogeneous solution of the binder before mixing. First, the dry powders were mixed using a shaker mill (Retsch MM 400) at 15 Hz for 20 minutes, before PVDF and NEP was added to the mixture. The final slurry was then mixed with a 7 mm steel ball an additional 40 minutes at 15 Hz, before the slurry was drop casted onto pre-cut carbon paper current collectors (Spectracarb 2050A-0550) with a diameter of 16 mm. Before being introduced into the glovebox, the cathodes were dried under vacuum at 120 °C for >3 h. The mass loadings of the active material varied between 1-2 mg/cm³. For preparation of the carbon black reference electrodes, the same procedure was performed, but with 90 wt% carbon black (45 mg), 10 wt% PVDF (5 mg) and 2 ml of NEP. The mass loadings of these were 0.5-1 mg/cm³.

Electrolyte mixing

The APC-THF electrolyte was prepared according to the procedure described by Byeon *et al*.[3] First, 4 ml THF (> 99.9%, inhibitor-free, Sigma Aldrich) was slowly added to 2.5 ml of 2 M phenyl magnesium chloride in THF (Sigma Aldrich) in a glass bottle while stirring. Secondly, 4 ml of 0.5 M $AlCl_3$ in THF (Sigma Aldrich) was carefully added to the solution, before the solution was left stirring overnight. The 0.4 M LiCl in APC-THF electrolyte was prepared by dissolving 0.0509 g LiCl (99.7%, VWR) in 3 ml of the prepared APC-THF. The mixture was left stirring for 24 h to completely dissolve the LiCl salt.

The preparation of 0.25 M $Mg(TFSI)_2$ 0.5M $MgCl_2$ in DME was based on earlier studies.[4-6] Ultradry $Mg(TFSI)_2$ (Solvionic, 99.5%, H_2O < 250 ppm) was further dried under vacuum at 240 °C in a vacuum chamber connected to the glovebox. Anhydrous $MgCl_2$ (Sigma, 99.9%), together with the electrolyte glass bottle and magnet was similarly dried at 150 °C for 15 h under vacuum. DME was dried with molecular sieves (UOP Type 3A) for > 48h. Typically, 0.8769 g $Mg(TFSI)_2$ and 0.2856 g $MgCl_2$ was mixed in 6 ml of dried DME using a syringe filter (Whatman R Puradisc, 0.2 mm, PTFE) to filter the DME, where the first 1 ml was discarded to avoid impurities from the filter. The resulting mixture was finally stirred 24 h.

0.5 M $Mg(BH_4)_2$ in THF was prepared according to Mohtadi *et al*.[7] In a typical procedure, 0.1080 g $Mg(BH_4)_2$ (Sigma, 95%) was dissolved in 4 ml THF (> 99.9%, inhibitor-free, Sigma Aldrich) in a glass bottle, by stirring overnight. The $Mg(BH_4)_2$ and THF was used as-received, and the glass bottle and Teflon magnet was dried at 150 °C for 15 h under vacuum.

The BMOC-DME preparation was based on the procedure described by Xu *et al*.[8] First, 0.004 g of MgO (99.99%, Sigma-Aldrich) was added to a glass bottle. Then, 128 ml of the anion receptor tris(2H-hexafluoroisopropyl) borate (THFPB), corresponding to 0.2048 g, was added. The THFPB has a melting point of 31 °C and was therefore first heated at 40 °C for 5 minutes on a hot plate to remove crystallized particles. Lastly, 2 ml of DME (99.5%, inhibitor-free, Sigma Aldrich) was added, and the electrolyte was stirred overnight. Prior to electrolyte preparation, the DME was dried using molecular sieves (UOP Type 3A°) for > 48 h. The dried DME was filtered through a syringe filter (Whatman R Puradisc, 0.2 mm, PTFE), where the first 1 ml was discarded to avoid impurities from the filter. The MgO and THFPB were used as-received.

Electrochemical measurements

To characterize the electrochemical performance of the prepared cathodes, Hohsen CR2016 coin cells were assembled in an argon filled glovebox (O_2 and H_2O levels < 0.1 ppm), with MXene or carbon black composites as the positive electrode material, Mg foil (Solution Materials) as the negative electrode, glass fibre separator (Whatman GF/A), a 0.3 mm stainless steel spacer and a total of 120 µl of one of the above-mentioned electrolytes. The Mg foil was polished with SiC sandpaper, cleaned with absolute ethanol and dried at 50 °C under vacuum > 2 h before being introduced to the glovebox, in order to remove oxide layers. The room temperature galvanostatic and potentiostatic cycling of the various cells were conducted on a Bio-Logic BCS-805 cycler in a temperature-controlled room at 20 °C. To test the cycling properties at elevated temperatures, a temperature chamber with a MACCOR 4200 cycler was used. Due to observed instability of the APC-THF electrolyte at 60 °C, the upper cut-off voltage was reduced to 1.9 V, as compared to 2.1 V for the room temperature cycling.

DFT calculations

The simulations were performed with the plane wave code Vienna *Ab Initio* Simulation package (VASP),[9-11] using the GGA functional PBEsol,[12] described by the projector augmented wave method (PAW). All calculations were performed at 0 Kelvin. The D2 method of Grimme[13] was used to correct for Van der Waals interactions, with a vdW radius of 15 Å and a global scaling factor of 0.75. 4x4x1 k-points were used to sample the Brillouin zone for the 3x3 super cells used for calculating the migration barriers, ref Figure S9 (a,b,c,d). 12x12x4 k-points were applied to the unit cells used for calculating voltages and Bader charges, ref Figure S9 (e,f). The k-points were generated with the Monkhorst Pack method. An energy of 650 eV was used for plane wave cut-off. The Methfessel-Paxton scheme was used to account for partial occupancies with a smearing width of 0.1 eV. The electronic ground state was converged to $1 \cdot 10^{-6}$ eV, while the conjugate gradient method was used to relax the structures to the forces were less than 0.01 eV $Å^{-1}$, unless otherwise stated.

The Climbing Image Nudged Elastic Band method (cNEB)[14-18] was used to find the migration energy barriers, relaxing the forces to less than 0.02 eV $Å^{-1}$ The RMM-DIIS quasi-Newton method was used for relaxing the forces for all systems, except for Mg on a single-layer of V_2CO_2 where the force based conjugate gradient method was used in addition due to convergence difficulties. 4 images were used for barriers on single-layers, and 3 images were used for barriers in multi-layer MXenes. The barriers were calculated for ions moving from a stable C-site to a metastable M-site, (Figure 4 and S9). These results were mirrored to give migration energy barrier profiles between two adjacent C-sites. Calculating the migration energy barriers directly between two C-sites was also tested for the multilayer system, showing for all cases that the minimum energy path went through the metastable M-site. However, some of the images did not relax to 0.02 eV Å-1, and the C-site to M-site approach was chosen instead.

Phonons for single-layer MXenes were calculated with VASP, using phonopy[19] for setting up and performing the calculations, and Sumo[20] to facilitate plotting. The ground states were relaxed to forces less than $1 \cdot 10^{-4}$ eV $Å^{-1}$ per atom with a quasi-Newton algorithm, and a 4x4x1 supercell (similar to Figure S9 b and d, but 4/3 times larger in the xy-plane and without Mg/Li) with 3x3x1 k-points. The electronic ground state was relaxed to $1 \cdot 10^{-8}$ eV. A 3x3x1 supercell for the phonon calculations was also attempted, but it proved infeasible as there were problems with an unstable phonon/negative frequency for V_2CO_2 in the M-point. Attempts at freezing in the phonon (performing geometric relaxation of V_2CO_2 with the unstable phonon given a certain amplitude), were not successful as the structure always relaxed back to the original ground state. However, V_2CO_2's unstable phonon disappeared when the supercell size was increased to 4x4x1. This unstable phonon was therefore attributed to size effects.

Bader charges were calculated with scripts from the Henkelmann group.[21-24] The charges were converged with respect to the fine FFT-grid, and 168x168x1008 grid points were used for $Ti_3C_2T_2$, while 192x192x1008 grid points for V_2CT_2. The super cells used for cNEB calculations (Figure S9 a, b, c and d) were relaxed with unit cell shape and ionic positions as free variables, but fixed volume, using a vacuum spacing of ~25 Å. Afterwards, Li/Mg/MgCl were relaxed onto the MXenes using a fixed volume and unit cell shape, but all other parameters free. For the cells used for calculating average voltages and Bader charges (Figure S9 e and f) all variables were free when relaxing. The

pseudopotentials supplied with the VASP package were used according to the recommendations of the Materials Project,[25] were Li had 3 valence electrons, Mg 8, C 4, O 6, F 7, Cl 7, Ti 10 and V 13 valence electrons. The initial geometries were based on data from [26, 27].

The voltages presented in Figure 5b were calculated according to the formula:

$$V = -\frac{E_{\text{intercalated MXene}} - E_{\text{Mg/Li}} - E_{\text{unintercalated MXene}}}{n_{\text{Mg/Li}}},$$

where $E_{\text{intercalated MXene}}$ is the energy for 100% intercalation (Figure S9 e and f), *i.e.* for $MgTi_3C_2T_2$, MgV_2CT_2, $LiTi_3C_2T_2$, LiV_2CT_2, $E_{\text{unintercalated MXene}}$ is the (fully relaxed) energy for $Ti_3C_2T_2$/ V_2CT_2 (Figure S9 e and f without any Li or Mg), $E_{\text{Mg/Li}}$ is the energy for Li/Mg in bulk metal state, and where $n_{\text{valency intercalation metal}}$ was 2 for Mg and 1 for Li. Mg and Li metal was computed and relaxed with the same settings as the MXenes, except that 10x10x10 k-points were used for a 2 atom unit cell with body centred cubic packing for Li, and 12x8x8 k-points were used for a 4 atom orthogonal unit cell with hexagonal close packed Mg.

The intercalation energy in Figure 5a was calculated for the setup used for calculating the energy barriers, *i.e.* 1/9th of the single-layer surface covered with Mg/Li, and 1/9th of interlayer-layer space intercalated with Mg/Li, as shown in Figure S9 a, b, c, and d. The following formula was used:

$$E_{intercalation} = E_{\text{intercalated MXene}} - E_{\text{Mg/Li}} - E_{\text{unintercalated MXene}}$$

The figures showing the simulation setups were made with VESTA.[28]

Supplementary figures and tables

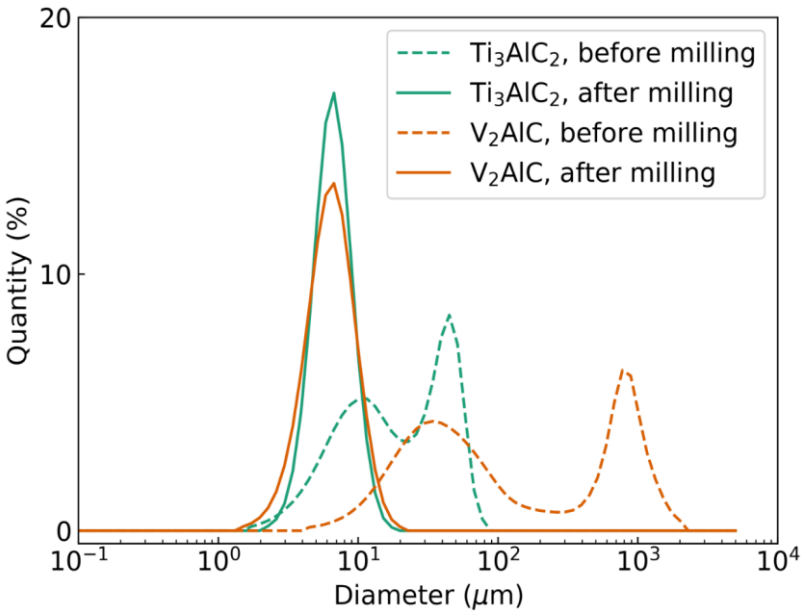

Figure S1 Particle size distribution from laser diffraction measurements of Ti_3AlC_2 and V_2AlC, before and after planetary milling at 300 rpm for 2 h and 4 h, respectively.

Table S1 EDX measurements from the two MAX phases before and after the etching. For simplicity, the elemental content is given relative to a unit cell value of 3 and 2 for the Ti_3AlC_2 and V_2AlC phases, respectively.

MXene	Ti/V	Al	O	F
Ti_3AlC_2	3	1.15	-	-
$Ti_3C_2T_x$	3	0.01	3.15	2.32
V_2AlC	2	1.22	-	-
V_2CT_x	2	0.10	0.63	0.95

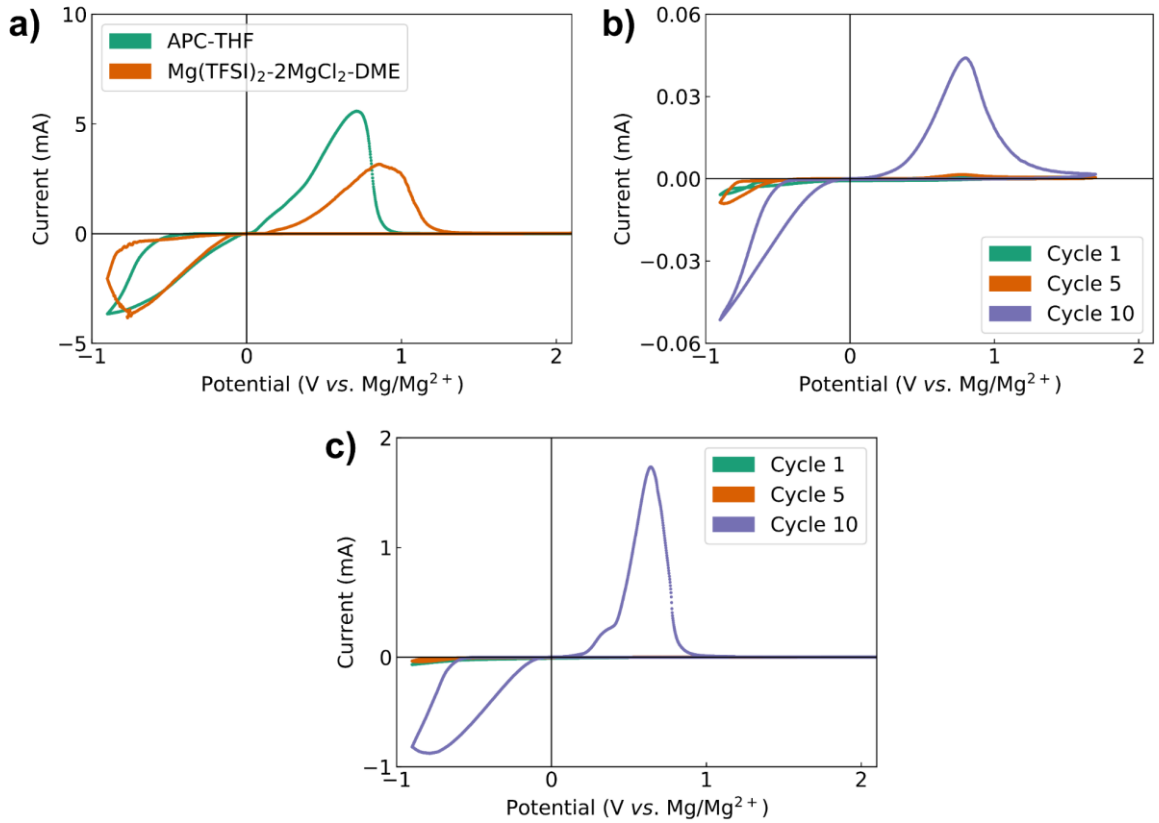

Figure S2 Cyclic voltammetry of all-phenyl complex in tetrahydrofuran (APC-THF) and $Mg(TFSI)_2$-$2MgCl_2$ in DME *vs.* a graphite disc electrode (a), $Mg(BH_4)_2$ in THF (b) and borate magnesium oxide complex in DME (BMOC-DME) (c). All demonstrates reversible Mg deposition and stripping. While (a) shows high current densities in the first cycle, (b) and (c) show decent current densities only after initial cycles. Due to the low cycling currents used throughout this work, 3-electrode cells showed that the electrolytes did not limit the cathode performance (data not shown).

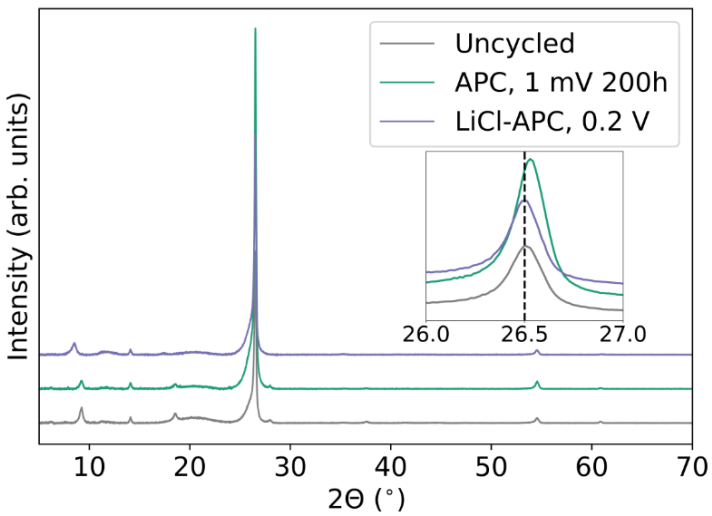

Figure S3 XRD of $Ti_3C_2T_x$ electrode before cycling (grey), after the potentiostatic hold step at 1 mV for 200 h with APC-THF electrolyte (cyan), and after being discharged to 0.2 V with APC-THF with 0.4 M LiCl (purple). The peak at 2Θ = 26.5° is assigned to the graphite current collector, shown in the inset.

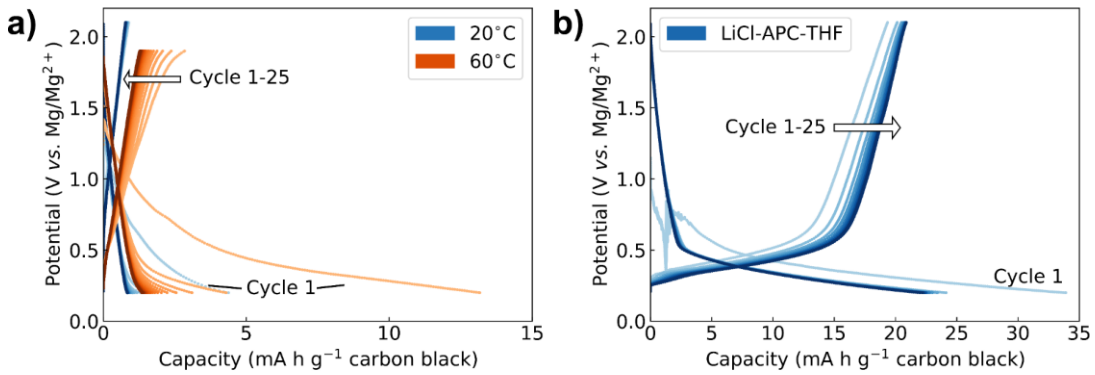

Figure S4 Voltage profiles of carbon black reference electrodes (90 wt% carbon black, 10 wt% PVDF) cycled with APC-THF at 20 °C and 60 °C (a), and APC-THF with 0.4 M LiCl (b).

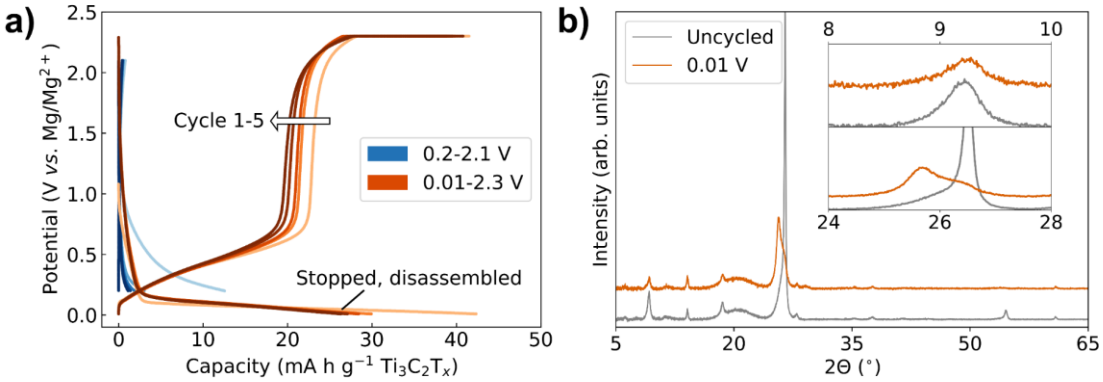

Figure S5 Voltage profiles of $Ti_3C_2T_x$ with BMOC-DME electrolyte, cycled at 0.2-2.1 V, and 0.01-2.3 V (a), before being stopped at 0.01 V for post mortem XRD (b), demonstrating a shift in the graphite peak (bottom plot in inset).

Figure S6 Signs of side reactions on the bottom steel casing after performing the 200 h hold step at 1 mV *vs.* Mg/Mg^{2+} with the APC-THF electrolyte, after being rinsed in THF.

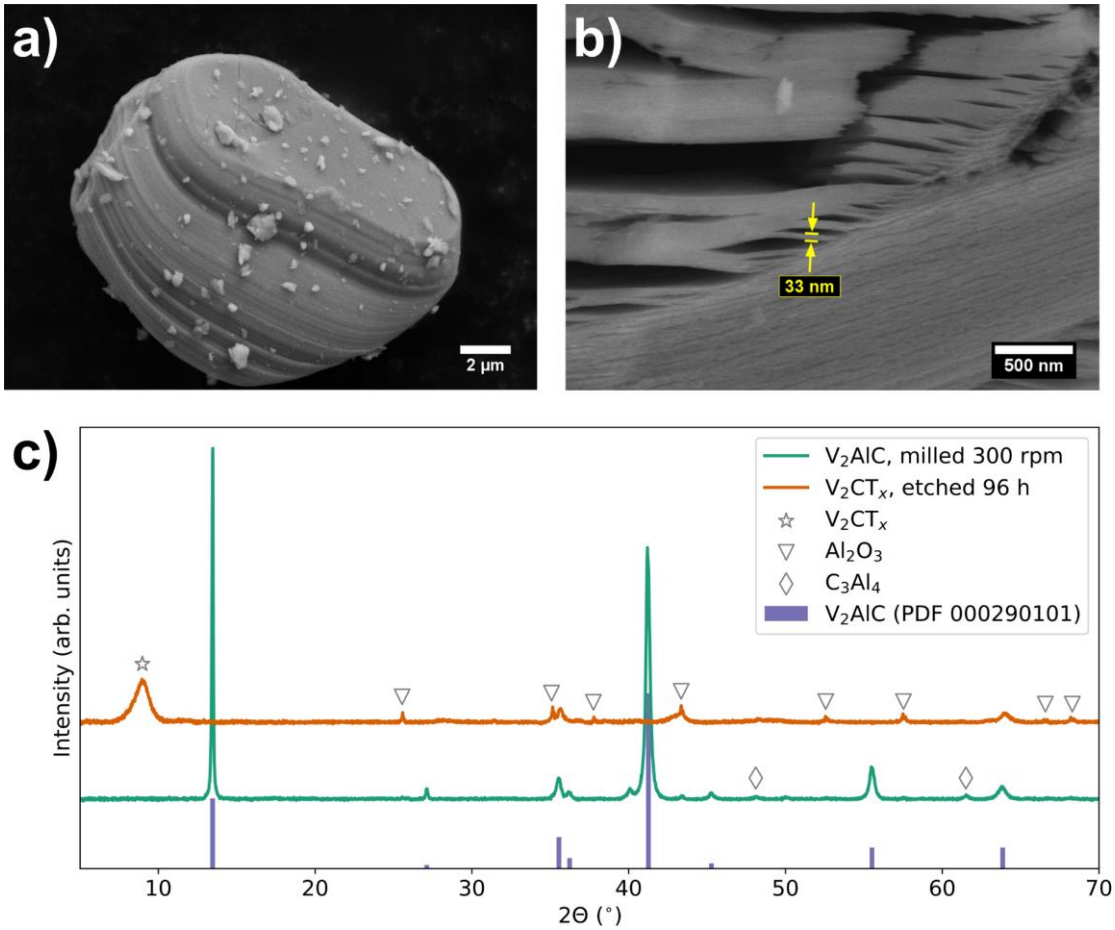

Figure S7 (a) V_2AlC MAX phase particle after milling at 300 rpm for 4 h. (b) V_2CT_x MXene, after etching for 96 h in 48 wt% HF. (c) XRD of both V_2AlC MAX phase and V_2CT_x MXene.

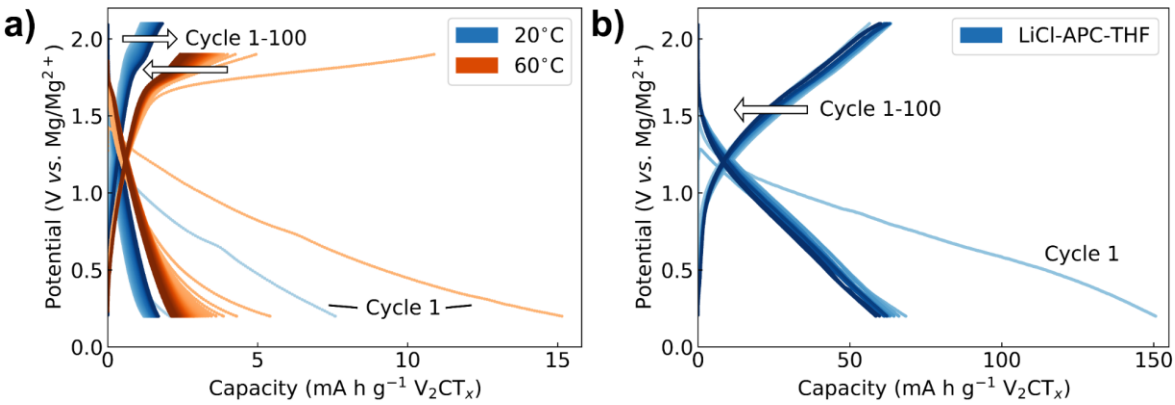

Figure S8 Voltage profiles of V_2CT_x with APC-THF electrolyte at 20 °C and 60 °C (a) and with APC-THF with 0.4 M LiCl (b).

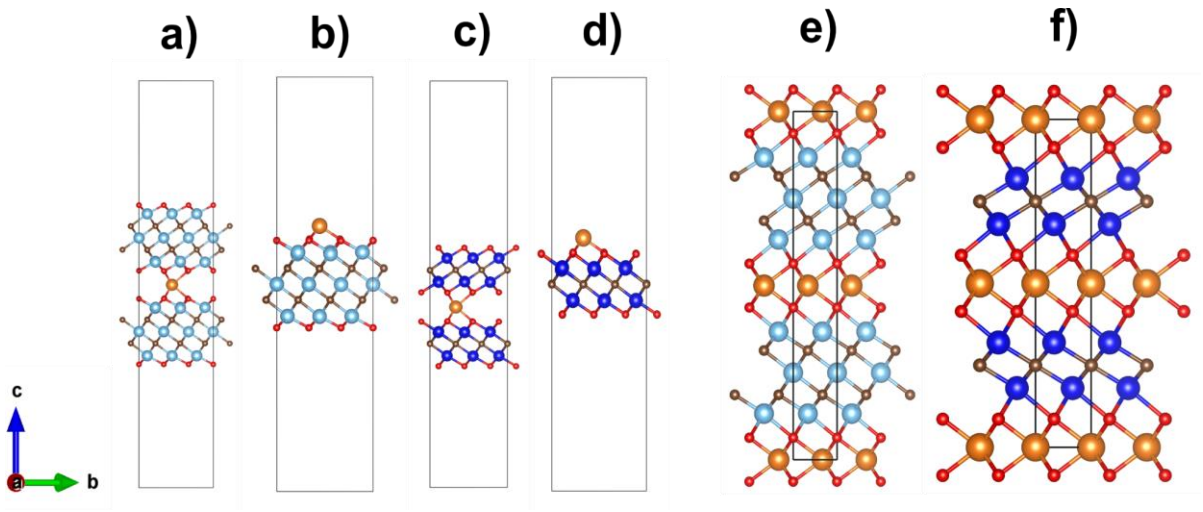

Figure S9 Side view of the different example unit cells used for DFT calculations. (e-f) was used for calculating the average voltage and Bader charges for multi-layer (ML) MXenes completely filled with Mg/Li. (a) and (c) were used for calculating the migration barrier in the fully charged limit for ML MXenes. Vacuum was added to avoid Mg^{2+}-Mg^{2+} interactions across the unit cells along the c-axis. (b) and (d) were used to calculate migration barriers in the fully charged limit for single-layer MXenes. Figure 4a shows top view of the migration barrier calculations.

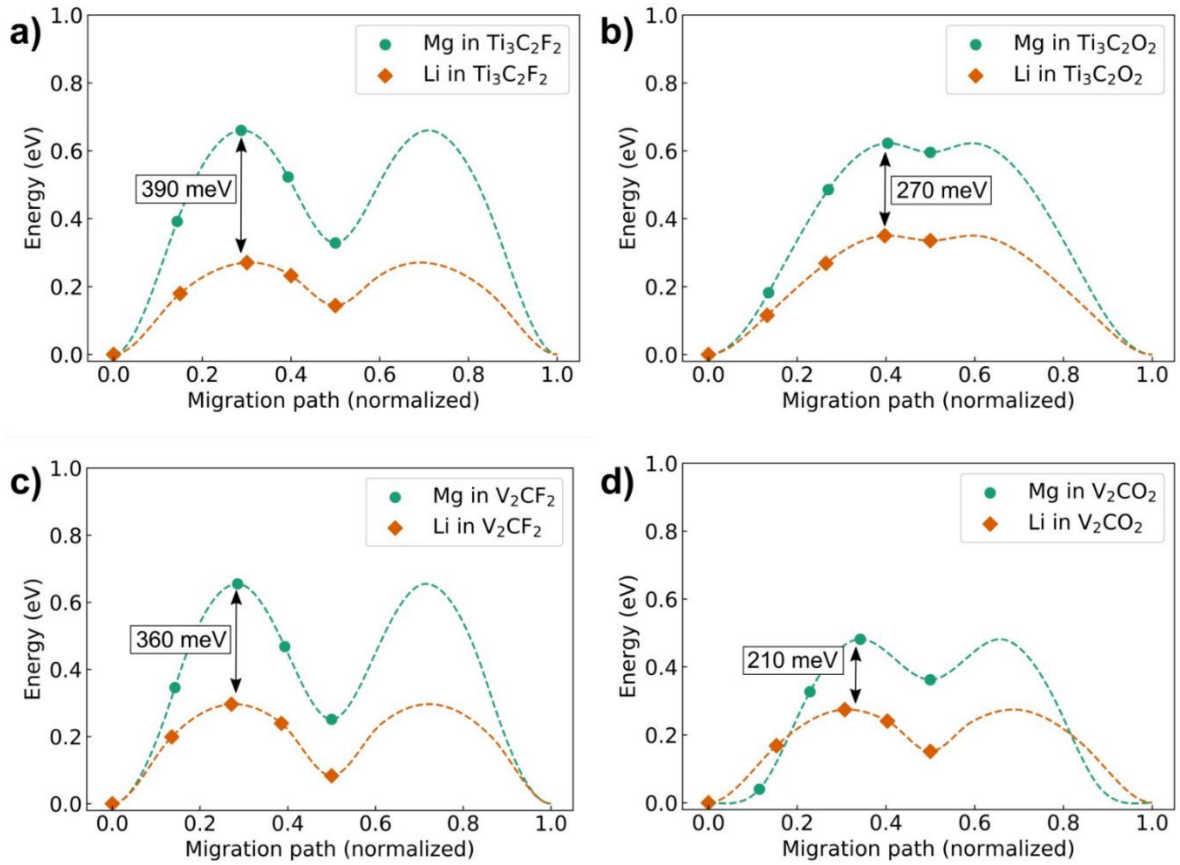

Figure S10 Climbing Image Nudge Elastic Band (cNEB) profiles of multi-layer $Ti_3C_2F_2$ (a), $Ti_3C_2O_2$ (b), V_2CF_2 (c) and V_2CO_2 (d) for the migration of Mg (circles) and Li (diamonds) from C-site to C-site. The stable C-site is with Li/Mg between to carbon atoms (Figure S9 and 4a). The metastable M-site

halfway along the migration path is with Li/Mg between two Ti/V atoms. The cNEB calculations were performed with three images between the C and M-site, to save computational cost and facilitate convergence. The migration path is normalized to ease the comparison, as the Mg migrates a longer path (more curved) than Li. The migration barrier difference between Mg and Li is noted in each panel.

Table S2 A comparison of the migration barriers of Mg-ions and Li-ions in various MXene structures, together with the relative differences in diffusion. Diffusion is proportional to the hopping probability, which again is proportional to $\exp(-E_a/k_bT)$, where E_a is the migration barrier, k_b is the Boltzmann constant and T is the temperature. The relative differences in diffusion (D_{Li}/D_{Mg}) is therefore calculated from the relative differences in $\exp(-E_a/k_bT)$ for Li and Mg at T = 22 °C.

MXene	E_a^{Li}	$\exp(-E_a^{Li}/k_bT)$	E_a^{Mg}	$\exp(-E_a^{Mg}/k_bT)$	D_{Li}/D_{Mg}
$Ti_3C_2F_2$	270	$2.44 * 10^{-5}$	660	$5.30 * 10^{-12}$	$4.60 * 10^{6}$
$Ti_3C_2O_2$	350	$1.05 * 10^{-6}$	622	$2.36 * 10^{-11}$	$4.45 * 10^{4}$
V_2CF_2	296	$8.77 * 10^{-6}$	655	$6.45 * 10^{-12}$	$1.36 * 10^{6}$
V_2CO_2	274	$2.08 * 10^{-5}$	482	$5.82 * 10^{-9}$	$3.57 * 10^{3}$

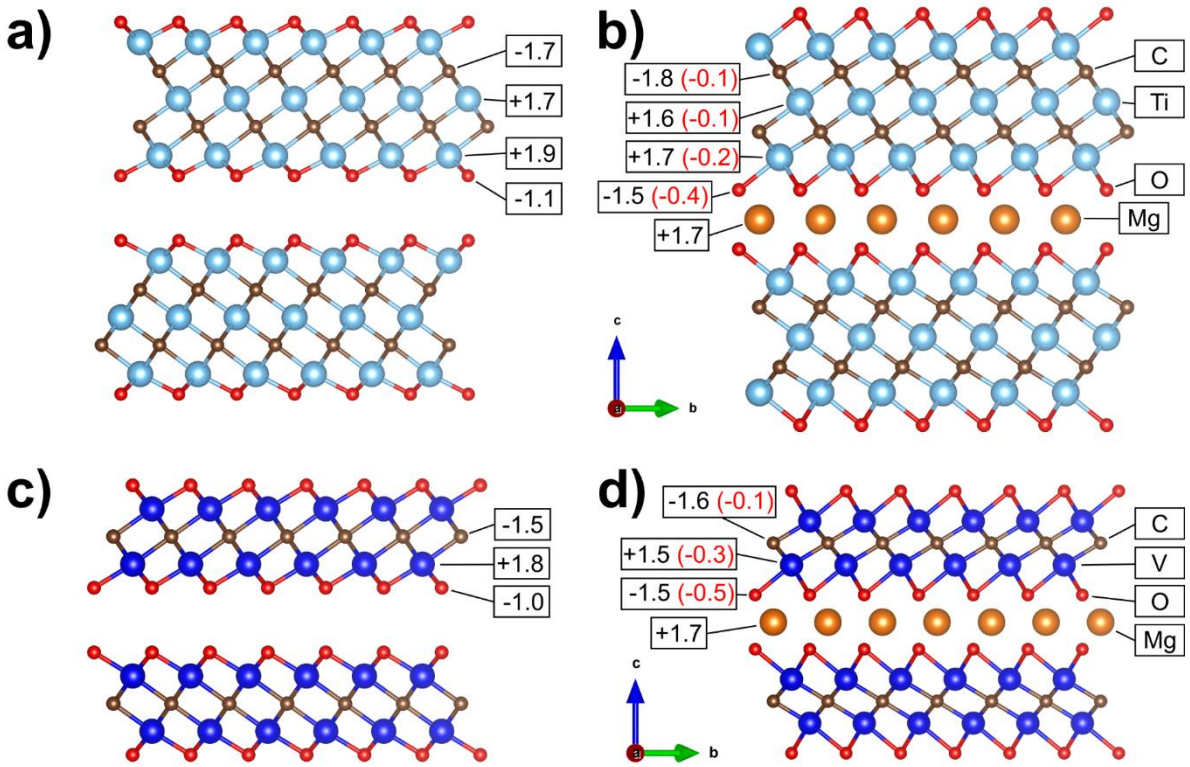

Figure S11 Bader charge analysis[21] of $Ti_3C_2O_2$ (a, b) and V_2CO_2 (c, d) MXene before Mg intercalation (a, c) and after (b, d). Bader charge analysis assigns the cumulative electronic charge density to atoms, where the atom separation is defined by a minimum in the electronic charge density landscape. The charge change after Mg intercalation is noted in parenthesis. The unit cell used for the Bader charge calculation is shown in Figure S9 e-f.

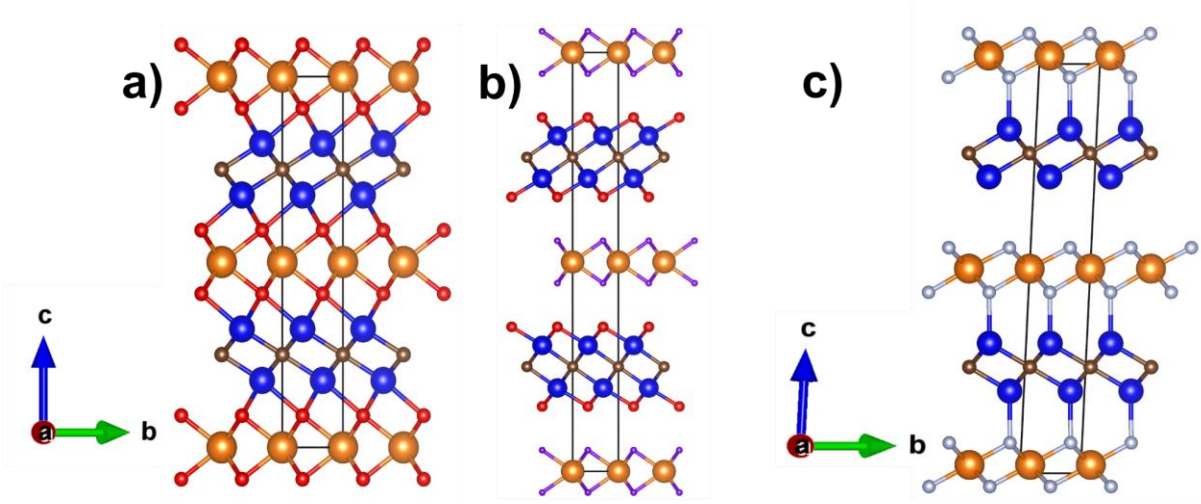

Figure S12 Visualization of the differences between introducing Mg (orange) into the V_2CT_2 MXene with the three different termination groups: V_2CO_2 (a), $V_2C(OH)_2$ (b) and V_2CF_2 (c). The different atoms are shown as blue (V), brown (C), red (O), grey (F) and purple (H) balls. Notably, the geometrically relaxed structures suggest that the Mg^{2+} reacts with the hydroxyl and fluorine termination groups, forming MgH_2 (b) and MgF_2 (c), respectively.

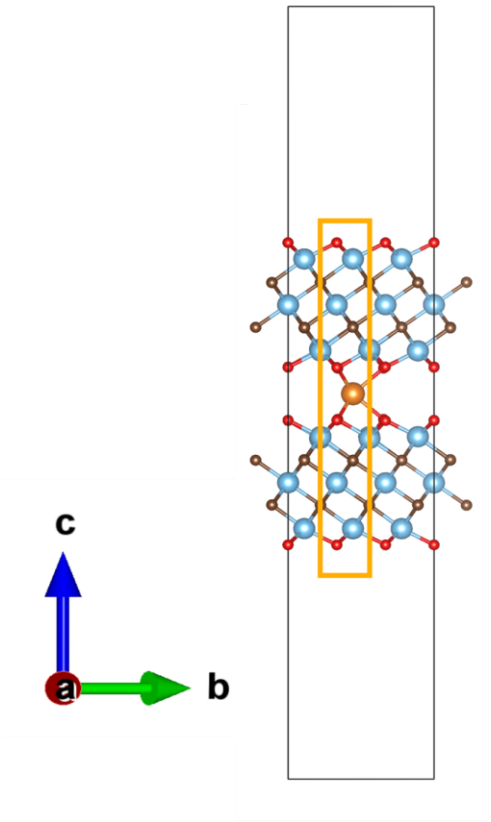

Figure S13 Close up of Figure S9 (a), with a rectangle to emphasize the stacking used for all the calculations.

Table S3 A summary of the intercalation energies, voltages and cNEB migration barriers calculated for Li and Mg intercalation into $Ti_3C_2T_2$ and V_2CT_2 MXenes with various termination groups (T). The unit cells used for these calculations are shown in Figure S9.

Structure	Intercalation Energy (eV)		Voltage (V *vs.* Mg/Mg^{2+} or Li/Li^+)	cNEB migration barriers (meV)	
	Multi-layer	Single-layer	Multi-layer	Multi-layer	Single-layer
$Ti_3C_2F_2$-Li	-1.63	-0.69	0.68	270	292
$Ti_3C_2F_2$-Mg	-0.37	1.85	-1.29	660	11
Ti_3C_2(OH)2-Mg	-	1.44	-0.05	-	24
$Ti_3C_2O_2$-Li	-3.19	-2.38	3.03	350	367
$Ti_3C_2O_2$-Mg	-3.87	-1.52	1.26	622	808
$Ti_3C_2O_2$-MgCl	-	-	-	-	351
V_2CF_2-Li	-2.19	-1.29	1.12	296	256
V_2CF_2-Mg	-1.60	0.87	-0.05	655	351
$V_2C(OH)_2$-Mg	-	0.92	-0.47	-	-
V_2CO_2-Li	-3.75	-2.85	3.28	274	248
V_2CO_2-Mg	-4.83	-2.12	1.45	482	640
V_2CO_2-MgCl	-	-	-	-	269

Table S4 Summary of the total energies taken directly from the VASP output for the structures shown in Figure S9, with various degrees of Mg filling. The Mg site between two carbon atoms is referred to as the C-site, whereas the Mg site between two metal atoms (Ti/V) is referred to as the M-site. The bulk structure refers to the unit cells shown in Figure S9 e-f, whereas multi-layer refers to the ones in Figure S9 a and c. The total energies for Li and Mg metal are given for one bulk atom.

Structure	Bulk (S9 e,f) (eV)		Multi-layer (S9, a, c) (eV)			Single-layer (eV) (S9, b, d)		
	0% Mg	100% Mg on C-site	0% Mg	1/9 Mg on C-site	1/9 Mg on M-site	0% Mg	1/9 Mg on C-site	1/9 Mg on M-site
$Ti_3C_2F_2$-Li	-125.78	-131.33	-1131.11	-1134.84	-1134.70	-565.15	-567.94	-567.76
$Ti_3C_2F_2$-Mg	-125.78	-128.85	-1131.11	-1133.54	-1133.21	-565.15	-565.36	-565.35
Ti_3C_2(OH)2-Mg	-150.26	-154.16	-	-	-	-674.82	-675.42	-675.43
$Ti_3C_2O_2$-Li	-136.91	-147.16	-1231.22	-1236.51	-1236.18	-615.12	-619.59	-619.25
$Ti_3C_2O_2$-Mg	-136.91	-146.08	-1231.22	-1237.16	-1236.56	-615.12	-618.70	-618.20
$Ti_3C_2O_2$-MgCl	-	-	-	-	-	-615.12	-622.80	-622.47
V_2CF_2-Li	-86.75	-93.18	-761.81	-766.10	-766.01	-380.46	-383.85	-383.72
V_2CF_2-Mg	-86.75	-90.68	-761.81	-765.47	-765.22	-380.46	-381.65	-381.49
$V_2C(OH)_2$-Mg	-109.79	-112.03	-	-	-	-492.45	-493.58	-493.58
V_2CO_2-Li	-95.96	-106.72	-862.63	-868.47	-868.32	-430.77	-435.72	-435.53
V_2CO_2-Mg	-95.96	-105.88	-862.63	-869.51	-869.15	-430.77	-434.95	-434.60
V_2CO_2-MgCl	-	-	-	-	-	-430.77	-438.92	-438.72
Li metal	-2.10		-			-		
Mg metal	-2.06		-			-		

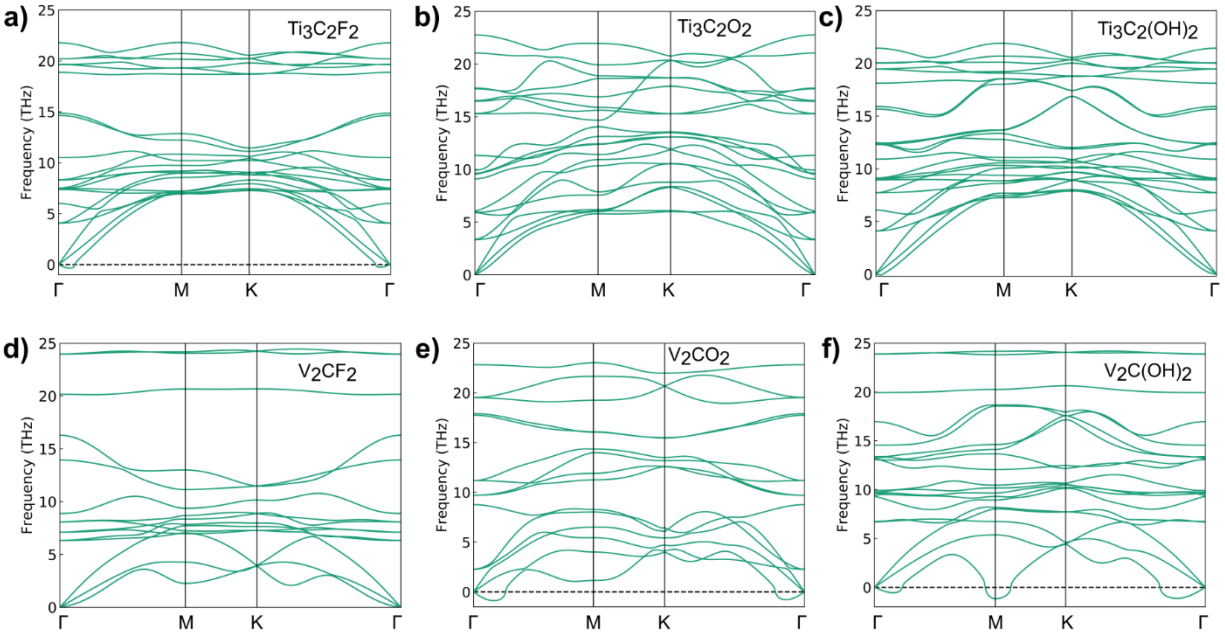

Figure S14 Calculated phonon dispersion diagrams for $Ti_3C_2F_2$ (a), $Ti_3C_2O_2$ (b), $Ti_3C_2(OH)_2$ (c), V_2CF_2 (d), V_2CO_2 (e) and $V_2C(OH)_2$ (f) using a 4x4x1 single-layer supercell. All of the MXenes depicted stable phonons in the Γ, M and K points, except for $V_2C(OH)_2$ which showed dynamic instability in the M point. This agrees well with previous reports for Ti_3CT_2.[29] It should be noted that $V_2C(OH)_2$ was stable in the M point when a 3x3x1 supercell was used. The apparent dependency of the stability of the M point on the supercell size may explain the discrepancy to a recent study, where they reported that $V_2C(OH)_2$ is dynamically stable and V_2CO_2 is unstable.[30]

References:

1. M. Naguib, J. Halim, J. Lu, K. M. Cook, L. Hultman, Y. Gogotsi and M. W. Barsoum, *Journal of the American Chemical Society*, 2013, **135**, 15966-15969.
2. M. Matsui, *Journal of Power Sources*, 2011, **196**, 7048-7055.
3. A. Byeon, M.-Q. Zhao, C. E. Ren, J. Halim, S. Kota, P. Urbankowski, B. Anasori, M. W. Barsoum and Y. Gogotsi, *ACS Applied Materials & Interfaces*, 2017, **9**, 4296-4300.
4. *United States Pat.,* US20130252112A1, 2013.
5. T. Gao, S. Hou, F. Wang, Z. Ma, X. Li, K. Xu and C. Wang, *Angewandte Chemie International Edition*, 2017, **56**, 13526-13530.
6. I. Shterenberg, M. Salama, H. D. Yoo, Y. Gofer, J.-B. Park, Y.-K. Sun and D. Aurbach, *Journal of The Electrochemical Society*, 2015, **162**, A7118-A7128.
7. R. Mohtadi, M. Matsui, T. S. Arthur and S.-J. Hwang, *Angewandte Chemie International Edition*, 2012, **51**, 9780-9783.
8. H. Xu, Z. Zhang, Z. Cui, A. Du, C. Lu, S. Dong, J. Ma, X. Zhou and G. Cui, *Electrochemistry Communications*, 2017, **83**, 72-76.
9. G. Kresse and J. Furthmüller, *Computational Materials Science*, 1996, **6**, 15-50.
10. G. Kresse and J. Furthmüller, *Physical Review B*, 1996, **54**, 11169-11186.
11. G. Kresse and J. Hafner, *Physical Review B*, 1994, **49**, 14251-14269.
12. G. I. Csonka, J. P. Perdew, A. Ruzsinszky, P. H. T. Philipsen, S. Lebègue, J. Paier, O. A. Vydrov and J. G. Ángyán, *Physical Review B*, 2009, **79**, 155107.

13. S. Grimme, *Journal of Computational Chemistry*, 2006, **27**, 1787-1799.
14. G. Henkelman, G. Jóhannesson and H. Jónsson, in *Theoretical Methods in Condensed Phase Chemistry*, ed. S. D. Schwartz, Springer Netherlands, Dordrecht, 2002, DOI: 10.1007/0-306-46949-9_10, pp. 269-302.
15. G. Henkelman and H. Jónsson, *The Journal of Chemical Physics*, 2000, **113**, 9978-9985.
16. G. Henkelman, B. P. Uberuaga and H. Jónsson, *The Journal of Chemical Physics*, 2000, **113**, 9901-9904.
17. H. Jónsson and G. J. W. Mills, Karsten, in *Classical and Quantum Dynamics in Condensed Phase Simulations*, 2000, DOI: 10.1142/9789812839664_0016, pp. 385-404.
18. D. Sheppard, R. Terrell and G. Henkelman, *The Journal of Chemical Physics*, 2008, **128**, 134106.
19. A. Togo and I. Tanaka, *Scripta Materialia*, 2015, **108**, 1-5.
20. A. Ganose, A. Jackson and D. Scanlon, *Journal of Open Source Software*, 2018, **3**, 717.
21. G. Henkelman, A. Arnaldsson and H. Jónsson, *Computational Materials Science*, 2006, **36**, 354-360.
22. E. Sanville, S. D. Kenny, R. Smith and G. Henkelman, *Journal of Computational Chemistry*, 2007, **28**, 899-908.
23. W. Tang, E. Sanville and G. Henkelman, *Journal of Physics: Condensed Matter*, 2009, **21**, 084204.
24. M. Yu and D. R. Trinkle, *The Journal of Chemical Physics*, 2011, **134**, 064111.
25. A. Jain, S. P. Ong, G. Hautier, W. Chen, W. D. Richards, S. Dacek, S. Cholia, D. Gunter, D. Skinner, G. Ceder and K. A. Persson, *APL Materials*, 2013, **1**, 011002.
26. M. Khazaei, M. Arai, T. Sasaki, M. Estili and Y. Sakka, *Physical Chemistry Chemical Physics*, 2014, **16**, 7841-7849.
27. H. D. Yoo, Y. Liang, H. Dong, J. Lin, H. Wang, Y. Liu, L. Ma, T. Wu, Y. Li, Q. Ru, Y. Jing, Q. An, W. Zhou, J. Guo, J. Lu, S. T. Pantelides, X. Qian and Y. Yao, *Nature Communications*, 2017, **8**, 339.
28. K. Momma and F. Izumi, *Journal of Applied Crystallography*, 2011, **44**, 1272-1276.
29. T. Hu, J. Wang, H. Zhang, Z. Li, M. Hu and X. Wang, *Physical Chemistry Chemical Physics*, 2015, **17**, 9997-10003.
30. A. Champagne, L. Shi, T. Ouisse, B. Hackens and J.-C. Charlier, *Physical Review B*, 2018, **97**, 115439.